

Fermi level engineering in $\text{Mn}_2\text{Ru}_x\text{Ga}$ thin films by the variation of Mn and Ru content

K.E. Siewierska,^{1,*} G. Atcheson,¹ A. Jha,¹ K. Esien,² R. Smith,¹ S. Lenne,¹
N. Teichert,¹ J. O'Brien,¹ J.M.D. Coey,¹ P. Stamenov,¹ and K. Rode¹

¹*School of Physics and CRANN, Trinity College Dublin, Ireland*

²*Queen's University Belfast, Northern Ireland, United Kingdom*

(Dated: March 4, 2022)

Variation of Mn content in $\text{Mn}_2\text{Ru}_x\text{Ga}$ thin films influences chemical disorder and crystal structure, which strongly influence material properties. $\text{Mn}_y\text{Ru}_x\text{Ga}$ thin films with $1.2 < y < 2.6$ for $x = 0.5, 0.7$ and 0.9 were deposited by DC magnetron sputtering onto MgO (100) to investigate the influence of composition on magnetic order, magneto-transport and spin polarisation. Variation of Mn content was found to manipulate the population of Mn^{4c} sites. The z-projection of the Mn^{4c} sublattice moment was found to be $2.0 \mu_B$ per unit cell. Molecular mean field theory model was used to fit thermal net magnetisation data and extract Weiss coefficients and Heisenberg exchange energies. Comparison of anomalous Hall effect and SQUID magnetometry loops suggest canting of the net moment relative to the anisotropy axis in zero field. The origin of the canting is hypothesised to be due to non-collinearity of the Mn^{4c} sublattice moments, via a competing exchange mechanism between negative nearest and positive next-nearest intra-sublattice interactions. Addition of Mn onto the $4c$ site raises the sublattice magnetisation and enhances the efficiency of spin-orbit scattering hence increasing the anomalous Hall angle up to 2 %. For films with $x = 0.5$, the Hall angle varies linearly with spin polarisation and does not vary strongly with Mn content.

I. INTRODUCTION

Half-metallic compensated ferrimagnets also known as zero-moment half-metals (ZMHM), proposed by van Leuken and de Groot in 1995¹, are ideal candidates for applications in spintronic devices. These materials offer many advantages over their half-metallic ferromagnetic counterparts as well as antiferromagnets (AFMs)². The first member of ZMHM material class was the Heusler alloy $\text{Mn}_2\text{Ru}_x\text{Ga}$ which is a 21 valence electron compensated ferrimagnet with high polarisation in thin film form³. Other members of this class have been demonstrated in thin film⁴ and in bulk⁵. $\text{Mn}_2\text{Ru}_x\text{Ga}$ (MRG) crystallises in a cubic inverted full-Heusler structure (XA), space group $F\bar{4}3m$, with two crystallographically inequivalent magnetic Mn sites with $4a$ and $4c$ Wyckoff positions.

Highly textured MRG thin films are grown epitaxially on single crystal MgO (001) by DC magnetron sputtering. A small (≈ 1 %) tetragonal distortion due to the biaxial substrate strain induces perpendicular magnetic anisotropy of the net moment.³ The in-plane lattice parameter (a) is constrained by the substrate while the out-of-plane parameter (c) varies with Ru content. A small net magnetic moment in MRG is due to the compensating effect of antiferromagnetically coupled inequivalent Mn magnetic sublattices. At compensation, the net moment vanishes and hence magnetically the material resembles an antiferromagnet, while half-metallicity preserves high spin polarisation of up to 60 %³ in MRG as measured by PCAR. This leads to immunity to externally applied fields and absence of demagnetising fields. As the net moment tends to zero, anisotropy field becomes large, therefore high frequency spin dynamics and low Gilbert damping can be achieved. For MRG, maximum zero-applied-field resonance frequency ≈ 160 GHz and Gilbert damping $\alpha \approx 0.02$ have been demonstrated.^{6,7}

MRG also offers efficiency and ease of detection and manipulation of the magnetic state. Remarkably efficient generation of spin-orbit fields $\mu_0 H_{\text{eff}}$ was measured in single-layers

of MRG, where $\mu_0 H_{\text{eff}}$ approaches $0.1 \times 10^{-10} \text{ T m}^2 / \text{A}$ in the low-current density limit. This is almost a thousand times the Oersted field and one to two orders of magnitude greater than $\mu_0 H_{\text{eff}}$ in heavy metal/ferromagnet bilayers⁸. Transport in MRG is dominated by the Mn^{4c} sublattice which has a non-vanishing moment at compensation. This allows for observation of magnetic domains in MRG close to compensation by MOKE⁹. Most recent results demonstrate thermal single-pulse toggle switching in MRG, which is the first non-Gd based material to exhibit this effect^{10,11}. MRG based magnetic tunnel junctions offer a practical solution to the current problem of chip-to-chip generation and detection of electromagnetic radiation in the 0.3 THz - 3 THz frequency range, known as the THz gap.^{6,12}

Inductively coupled plasma mass spectroscopy (ICP-MS) measurements of composition of MRG thin films deposited by co-sputtering from a Mn_2Ga and Ru targets, the final Mn/Ga ratio may vary between 1.6 - 1.9.¹³ The DFT calculations show that reducing the Mn content on the MRG can give rise to Mn - Ga antisite defects, i.e. placing a Ga atom on an Mn site. Mn^{4a} - Ga antisite defects were found to leave one unbound electron and hence provide electronic doping to raise the position of the Fermi level. Further study showed that Mn^{4a} - Ga antisites are also crucial to opening of the spin gap in DOS, explaining the non-volume conserving strain and finding the correct ground states of MRG as a function of Ru concentration. Findings indicate that the site disorder is promoted by reducing the Mn occupancy on the $4a$ sites and according to calculations the ideal Mn/Ga ratio 1.4. Previous results also show higher Ru content increases tetragonal distortion of the crystal unit cell, quantified with the c/a ratio, as well as improve the wetting of the film on MgO and reduce the Anomalous Hall angle.^{6,13,14}

In this work we aim to prepare MRG thin films with varying the Mn and Ru content and investigate the impact of the composition on crystal structure, magnetic order and magneto-transport properties such as Anomalous Hall angle and spin-

polarisation. The MRG thin film compositions were calculated from sputtering rates of the targets used and are summarised in Table I. To model the temperature dependence of the net magnetisation and extract Heisenberg exchange coefficients, Weiss molecular mean field model for a 2D two sublattice ferrimagnet was used.

Series 1	Series 2	Series 3
Mn _{2.2} Ru _{0.5} Ga	Mn _{2.0} Ru _{0.7} Ga	Mn _{1.8} Ru _{0.9} Ga
Mn _{2.4} Ru _{0.5} Ga	Mn _{2.2} Ru _{0.7} Ga	Mn _{2.0} Ru _{0.9} Ga
Mn _{2.6} Ru _{0.5} Ga	Mn _{2.4} Ru _{0.7} Ga	Mn _{2.2} Ru _{0.9} Ga

TABLE I. Compositions of the thin films derived from sputtering rates, where Mn is varied in three Ru series. All films show compensation, with the exception of Mn_{2.2}Ru_{0.5}Ga with $T_{\text{comp}} < 0$ K.

II. METHODOLOGY

Epitaxial thin films of MRG were grown by DC magnetron sputtering, using our Shamrock sputtering system, on 10×10 mm² (100) MgO substrates. The films were co-sputtered in argon from three 75 mm targets of Mn₂Ga, Ru and either MnGa or Mn₃Ga onto the substrate maintained at 350 °C. This allows for the variation of Mn content of MRG. The films had an average thickness of 50 nm and were capped in-situ with a 3 nm layer of AlO_x deposited at room temperature in order to prevent oxidation. Composition analysis was performed by energy-dispersive X-ray spectroscopy (EDX).

A Bruker D8 HighRes X-ray diffractometer with a copper tube emitting K α X-rays with wavelength 154.06 pm and a double-bounce Ge [220] monochromator was used to determine the diffraction patterns of the thin films. Low angle X-ray reflectivity was measured using a Panalytical X'Pert Pro diffractometer, and thickness was found by fitting the interference pattern using X'Pert Reflectivity software.

Low field AHE measurements were performed in a 1 T GMW electromagnet system in ambient conditions. Silver wires were cold-welded to the thin films with indium and the current used was 5 mA. High field measurements were performed in a Quantum Design Physical Property Measurement System (PPMS) which has a maximum field of 14 T. The films were contacted with silver paint. The 4-point Van der Pauw method was used to determine Hall and longitudinal resistivity of the materials.

Point contact Andreev reflection (PCAR) measurements were also performed in PPMS using mechanically-sharpened Nb tip. The landing of tip onto the sample surface is carefully controlled by an automated vertical attocubeTM piezo stepper. Two horizontal attocubeTM piezo steppers are used to move the sample in laterally to probe the pristine area of sample. The differential conductance spectra were fitted using a modified Blonder-Tinkham-Klapwijkv (m-BTK) model, as detailed elsewhere^{15,16}.

Measurements of the magnetisation with a magnetic field applied perpendicular or parallel to the surface of the films were carried out using a 5 T Quantum Design SQUID. Hysteresis loops were measured in fields up to 5 T at room tem-

perature. These data were corrected for the diamagnetism of the substrate. Thermal scans from 10 K to 400 K in zero field after saturation of the magnetisation at room temperature were used to determine the compensation temperatures of the films.

For Kerr imaging, a wide-field Kerr microscope from Evico magnetics with a 10×/0.25 objective lens was used. All loops have been measured with polar sensitivity and red LED light and a field applied out-of-plane. Faraday rotation was compensated for during the measurement using a feature which readjusts the analyzer position relative to a mirror reference.¹⁷ The sample was heated on the microscope stage with an attached heating element, a thermocouple and proportional-integral-derivative (PID) controller.

III. RESULTS AND DISCUSSION

The desirable characteristics of ZMHM thin films are tunable T_{comp} , high Curie temperature T_C , low moment over a wide range, perpendicular magnetic anisotropy and high spin polarisation at Fermi level. All MRG thin films were investigated for the above properties to understand how they depend on both Mn and Ru composition. Compositions of thin films were calculated by determining the sputtering rates of all targets. A simple model was used to predict how varying Mn content on a particular site changes the compensation temperature (T_{comp}). The T_{comp} of all films was determined using thermal scans of out-of-plane magnetisation in the absence of an applied field in the SQUID magnetometer.

Mn ^{4a} occupancy	T_{comp}	Mn ^{4c} occupancy	T_{comp}
Increase	Decrease	Increase	Increase
Decrease	Increase	Decrease	Decrease

TABLE II. Dependence of T_{comp} on the variation of Mn^{4a} and Mn^{4c} sublattice occupation in MRG from our model.

To predict how T_{comp} will be influenced with varying Mn content a simple model was used and it is summarised in Table II. Since the two sublattices are antiferromagnetically coupled, we consider the Mn^{4a} moment is negative and Mn^{4c} moment is positive. In a previous study it was shown that below T_C Mn^{4a} moment is almost constant whereas Mn^{4c} moment will vary linearly as a function of temperature.¹⁸ Therefore in our model, adding (reducing) moment of the Mn^{4c} sublattice is expected to raise (lower) T_{comp} . For the Mn^{4a} sublattice, addition (reduction) of Mn will increase (decrease) the sublattice moment, however since this moment is negative it results in a decrease (increase) of T_{comp} , i.e. it has the opposite effect on T_{comp} compared with Mn^{4c} sublattice.

The measured T_{comp} values in samples that had a compensation point in the range $0 < T_{\text{comp}} < T_C$ are shown in Figure 1, where they are plotted versus Mn and Ru contents. As shown in previous studies, Ru content raises T_{comp} .³ Within each Ru series, data shows increasing Mn content also increases T_{comp} . The data was fitted with a plane, with the x and y components corresponding to Mn and Ru contents, respectively. The coefficients of the x and y variables show that addition of one

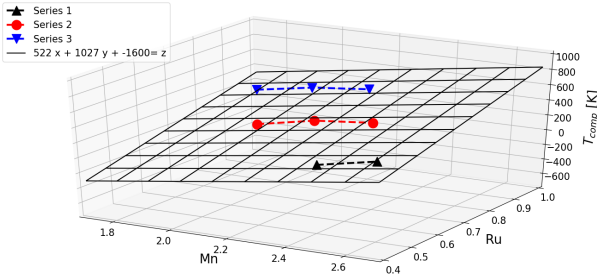


FIG. 1. T_{comp} of $\text{Mn}_y\text{Ru}_x\text{Ga}$ with variation of Mn and Ru content.

stoichiometric unit of Mn and Ru raises T_{comp} by 522 ± 65 K and 1027 ± 65 K, respectively. According to our model, an increase in T_{comp} implies that predominantly the Mn^{4c} sites are populated when more Mn content is increased. In this case, reducing Mn content in MRG does not promote the formation of Mn^{4a} - Ga antisites, instead there will be chemical disorder on the Mn^{4c} site. Figure 2 shows the variation of the z -

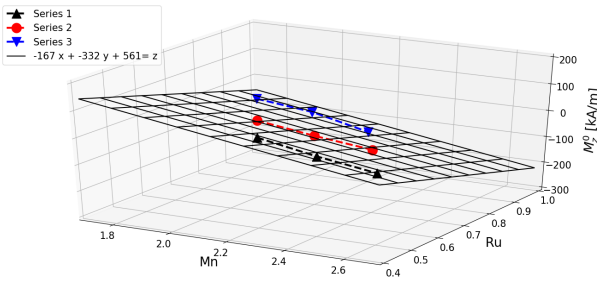


FIG. 2. Net magnetisation (z -component) values extrapolated to $T = 0$ K from SQUID magnetometry thermal scans of out-of-plane net moment in zero field versus Mn and Ru content.

component of net magnetisation extrapolated to $T = 0$ K (M_z^0) in zero field. The addition of an Mn atom causes an increase in the net moment of $1.0 \pm 0.1 \mu_B/\text{f.u.}$, and that Mn is mainly varied on $4c$ sites, the Mn^{4c} sublattice moment was found to be $2.0 \pm 0.2 \mu_B$ per unit cell. DFT calculations predicted $\approx 2.9 \mu_B$ per unit cell¹³, which is notably higher than our estimate. However this was expected since our measurements are of z -projection in zero field, which leads to an underestimation of the sublattice moment. The increase in net moment by adding a Ru atom was found to be $1.9 \pm 0.1 \mu_B/\text{f.u.}$, which is in close agreement to $2.0 \mu_B/\text{f.u.}$ from the Slater-Pauling curve¹⁹, which validates our model and compositions derived from sputtering rates.

Thermal scans of net magnetisation in zero field from SQUID were fitted using a 2D two sublattice ferrimagnet Weiss molecular mean field theory (MFT) model described by the system of linear equations

$$\begin{aligned} \mathbf{H}^{4a} &= n_W^{aa} \mathbf{M}^{4a} + n_W^{ac} \mathbf{M}^{4c} \\ \mathbf{H}^{4c} &= n_W^{ac} \mathbf{M}^{4a} + n_W^{cc} \mathbf{M}^{4c} \end{aligned} \quad (1)$$

where H^{4a} and H^{4c} are the internal molecular fields, M^{4a} and M^{4c} are the magnetisations of the $4a$ and $4c$ sublattices, which

are modelled by the Brillouin function and n_W^{aa} , n_W^{ac} and n_W^{cc} are Weiss coefficients. The Heisenberg exchange energies \mathcal{J} can be found using the expression

$$\mathcal{J}^{ij} = n_W^{ij} \rho \mu_0 (g \mu_B)^2 \quad (2)$$

where ρ is the number of atoms per unit cell volume, μ_0 is permeability of free space, g is the Landé g and μ_B is the Bohr magneton. It was assumed in the simulation that in the unit cell, the $4a$ and $4c$ sites are fully filled for Mn-excess compositions. For the Mn-deficient compositions, the occupancy of $4c$ sites was varied, while $4a$ site occupancy was unchanged. In the simulations the sublattice moments were fixed and for $\text{Mn}_2\text{Ru}_x\text{Ga}$ composition the $4c$ sublattice moment was taken to be $2.0 \pm 0.2 \mu_B$. The $4c$ sublattice moment was scaled according to composition for each sample. The net moment was known from SQUID and $4a$ sublattice moment was calculated by subtracting the net moment from $4c$ sublattice moment. The total angular momentum quantum numbers for both Mn sublattices, $J^{4a,4c}$, were expected to lie in the range $1.5 \leq J^{4a,4c} \leq 2.5$. For Mn in metal alloys, the quantum numbers strongly depend on the distances between the atoms and are difficult to determine. The quantum numbers $J^{4a,4c} = 1.9, 2.5$ were chosen because they best represented the data and lie within the range given above.

MOKE microscopy performed measures the Kerr rotation which for MRG is proportional to the magnetisation of the Mn^{4c} sublattice. Temperature dependent MOKE data was scaled to the M_z of the Mn^{4c} sublattice from the model to confirm that it is indeed proportional to it. Since MOKE was performed at higher temperatures than SQUID, so this data experimentally determined T_C and was used as a constraint for the MFT simulations. The SQUID data, MFT fits and MOKE data for the two compositions, $\text{Mn}_{2.0}\text{Ru}_{0.7}\text{Ga}$ and $\text{Mn}_{2.2}\text{Ru}_{0.9}\text{Ga}$, are shown in Figure 3.

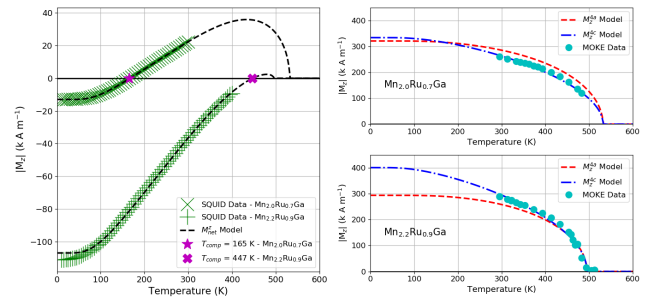


FIG. 3. $\text{Mn}_{2.0}\text{Ru}_{0.7}\text{Ga}$ and $\text{Mn}_{2.2}\text{Ru}_{0.9}\text{Ga}$ thin films. Left: MFT fit of net magnetisation versus temperature in zero field SQUID data. Right: Calculated Mn^{4a} and Mn^{4c} magnetisation curves with scaled MOKE data.

In the 2D two sublattice model, the sublattice magnetisations are always collinear. Table III summarises the input and output simulation parameters for the two compositions. For $\text{Mn}_{2.0}\text{Ru}_{0.7}\text{Ga}$ composition, the model agrees well with the SQUID data, $T_C = 536$ K which agrees with the MOKE data. The Heisenberg exchange energies \mathcal{J}^{aa} , \mathcal{J}^{ac} and \mathcal{J}^{cc} have the ratio $10.0 : -6.3 : 3.4$, similar to what was reported previously for MRG with a similar composition¹¹. Increasing Ru

Mn _{2.0} Ru _{0.7} Ga				Mn _{2.2} Ru _{0.9} Ga			
$J^{4a} = 1.9, J^{4c} = 2.5$		$J^{4a} = 1.6, J^{4c} = 2.5$		$J^{4a} = 1.6, J^{4c} = 2.5$		$J^{4a} = 1.6, J^{4c} = 2.5$	
$\rho^{4a} = 4.0, \rho^{4c} = 4.0$		$\rho^{4a} = 4.0, \rho^{4c} = 4.0$		$\rho^{4a} = 4.0, \rho^{4c} = 4.0$		$\rho^{4a} = 4.0, \rho^{4c} = 4.0$	
Mn4a: $M_z^0 = 321$ kA/m		Mn4a: $M_z^0 = 294$ kA/m		Mn4a: $M_z^0 = 294$ kA/m		Mn4a: $M_z^0 = 294$ kA/m	
Mn4c: $M_z^0 = 334$ kA/m		Mn4c: $M_z^0 = 334$ kA/m		Mn4c: $M_z^0 = 401$ kA/m		Mn4c: $M_z^0 = 401$ kA/m	
n_W^{aa}	686.0	\mathcal{J}^{aa}	34.39 meV	n_W^{aa}	649.0	\mathcal{J}^{aa}	32.54 meV
n_W^{ac}	-435.0	\mathcal{J}^{ac}	-21.81 meV	n_W^{ac}	-524.5	\mathcal{J}^{ac}	-26.30 meV
n_W^{cc}	234.2	\mathcal{J}^{cc}	11.74 meV	n_W^{cc}	81.1	\mathcal{J}^{cc}	4.07 meV

TABLE III. Summary of the total angular momenta ($J^{4a,4c}$), magnetisation at $T = 0$ K (M_z^0), extracted Weiss constants and Heisenberg exchange energies from MFT fitting for Mn_{2.0}Ru_{0.7}Ga and Mn_{2.2}Ru_{0.9}Ga thin films.

to $x = 0.9$ and Mn to $y = 2.2$ results in a decrease in intra-sublattice \mathcal{J}^{cc} energy and an increase in inter-sublattice exchange such that $|\mathcal{J}^{aa}| \approx |\mathcal{J}^{ac}|$, which is reflected in the ratio of exchange energies 10.0 : -8.1 : 1.3. The model fails to fit the data at low temperatures, which is a limitation of MFT, and $T_C = 495$ K in agreement with high temperature MOKE data.

In AHE measurements, the Hall resistance (R_{xy}) is proportional to the z-component of the Mn^{4c} sublattice magnetisation, i.e. $R_{xy} \propto M_z^{4c}$, because the Mn^{4c} sublattice electrons are mainly contributing to the Fermi level in the density of states and hence dominate the transport. The two types of contributions to AHE are extrinsic and intrinsic. Extrinsic contributions involve spin dependent scattering by impurities or large spin-orbit interaction defects via the side-jump or skew-scattering mechanism. The intrinsic contribution is the spin accumulation due to the non-collinear spin texture and Berry phase curvature. The ratio ρ_{xy}/ρ_{xx} gives the Anomalous Hall angle (θ_{AH}) which is a measure of spin dependent scattering.²⁰ Figure 4 shows AHE R_{xy} versus $\mu_0 H$ applied out of plane at

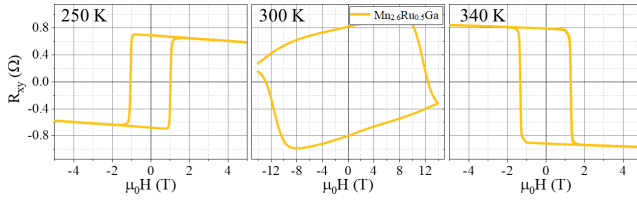


FIG. 4. AHE loops of Mn_{2.6}Ru_{0.5}Ga thin film, with $T_{comp} = 275$ K, measured at 250 K, 300 K and 340 K.

three various temperatures demonstrates that coercive field increases when the measurement temperature approaches the compensation point. The Anomalous Hall coefficient of the hysteresis loop changes when T_{comp} is crossed, which is consistent with a change of sign of spin polarisation of the carriers with respect to the net magnetisation.¹⁴ The AHE measurement at 300 K which is close to the compensation point of the sample shows the film has a huge anisotropy field > 12 T. The convention in this paper is that since Mn^{4c} sublattice moment dominates below T_{comp} , at positive $\mu_0 H$ the R_{xy} is set to be positive. Above T_{comp} Mn^{4a} sublattice moment is larger and at positive $\mu_0 H$, the sign of R_{xy} is negative.

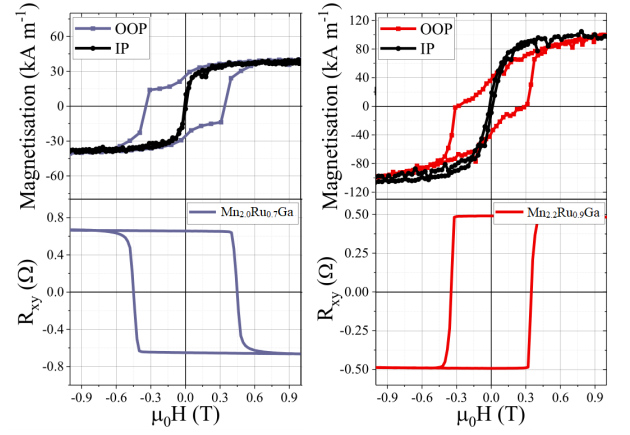


FIG. 5. Top panel: SQUID net magnetisation at 300 K with field applied out-of-plane (OOP) and in-plane (IP) relative to the sample surface. Bottom panel: Anomalous Hall effect measurements at 300 K.

Comparison of SQUID and AHE loops, shown in Figure 5, provides a further insight into the magnetism of the samples. In both samples, AHE loops have high remnance however the out-of-plane SQUID loops exhibit a "soft phase" at low fields and a hard phase with the same coercivity as observed in AHE. The apparent "soft phase" is hypothesised to originate from the canting of the net moment relative to the anisotropy axis. In Mn_{2.0}Ru_{0.7}Ga the canting is $\approx 37^\circ$, which suggests the sublattice moments are approximately collinear, consistent with the MFT data above. However, the canting angle at zero field for Mn_{2.2}Ru_{0.9}Ga is $\approx 69^\circ$. The apparent "soft component" of the net moment in the SQUID magnetometry data could arise from Mn^{4c} sublattice moments canting away from the anisotropy axis forming an easy cone, which is closed when an external field is applied. The easy cone angle could be only a few degrees to result in the canting of the net moment by tens of degrees. As a result, AHE cannot detect the very small canting of the Mn^{4c} sublattice and the loops are very square. The 2 sublattice MFT model does not allow for non-collinearity of sublattice moments, however the observed decrease in intra-sublattice \mathcal{J}^{cc} exchange energy could be due to increased competing positive and negative exchange on the Mn^{4c} sublattice²¹. Experimental techniques such as X-ray magnetic circular dichroism and/or neutron diffraction could confirm and investigate the sublattice non-collinearity further.

In the case of MRG, the tetragonal distortion of the unit cell reduces the cubic F43m group symmetry to the tetragonal I42m. The Mn^{4c} sublattice is non-centrosymmetric, which indicates the possibility of a non-collinear spin texture²² and large intrinsic contribution to AHE²³. From AHE and Van der Pauw measurements at 300 K, the transverse ρ_{xy} and longitudinal ρ_{xx} resistivities were obtained and θ_{AH} was calculated. In a previous study, it was reported that θ_{AH} is almost constant below T_C , hence the measurements were performed at 300 K.¹⁴ Figure 6 shows the spin polarisation and θ_{AH} as a function of Mn content and θ_{AH} versus spin polarisation. Initial increase of θ_{AH} is due to the increase of the magnetisation on the Mn^{4c} sublattice and an enhancement in the efficiency

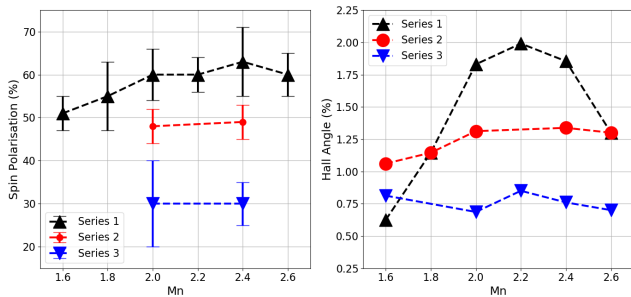


FIG. 6. Left: Spin polarisation measured by PCAR versus Mn content. Right: Anomalous Hall angle measured at 300 K versus Mn.

of spin dependent scattering. However increasing Mn content, raises T_{comp} towards 300 K and the Mn^{4c} sublattice magnetisation decreases. Therefore, θ_{AH} appears to reach a maximum and drops in films with $T_{\text{comp}} \approx 300$ K. Initial addition of Mn into MRG films in series 1 is accompanied by an improvement in crystalline quality and the chemical ordering in the films, giving rise to an increase in the spin polarisation from 51(4) % up to 63(8) %. The spin polarisation result is still quite far from the 100 % expected from an ideal half-metal. However, in reality this is close to the maximal value that can be observed using PCAR on Heusler alloy thin films and bulk samples³.

The maximal value of $\theta_{\text{AH}} = 2$ % for $\text{Mn}_{2.2}\text{Ru}_{0.5}\text{Ga}$ is an order of magnitude higher than in conventional ferromagnets measured at 300 K²⁴. Addition of Ru caused a decrease in θ_{AH} as shown in 6, which has been observed before¹⁴. Ru is the heaviest element in MRG with strongest spin-orbit coupling, hence increasing its concentration was initially expected to increase the spin-dependent scattering. The decrease in θ_{AH} as Ru is added to MRG is accompanied by a decrease in spin polarisation. This indicates that the Fermi Level is pushed up and out of the spin-gap in the density of states. Variation of Mn does not influence the spin polarisation strongly, which allows to maintain high spin polarisation but vary other properties such as T_{comp} .

IV. CONCLUSION

We have found that changing the Mn content in $\text{Mn}_2\text{Ru}_x\text{Ga}$ thin films results in the variation of the occupancy of the Mn^{4c} sites. This was deduced from a simple model which indicated that T_{comp} would increase when Mn was added onto the $4c$ site. From this the magnitude of the z-projection of the moment of Mn^{4c} sublattice in $\text{Mn}_2\text{Ru}_x\text{Ga}$ was found to be $2.0 \mu_B$ per unit cell, lower than $2.9 \mu_B$ per site calculated by DFT¹³. Addition of an Ru atom was found to increase the net moment by $2.0 \mu_B/\text{f.u.}$ which is consistent with the Slater-

Pauling curve¹⁹ and validates our model.

Two sublattice ferrimagnet molecular mean field theory model as used to fit thermal magnetisation curves of the net moment. Extraction of Weiss constants and Heisenberg exchange energies showed a reduction in \mathcal{J}^{cc} with increasing Ru content. SQUID and AHE hysteresis loops for the out-of-plane geometry for all Ru series show a good agreement in coercive fields. The striking difference is that the AHE loops are very square, but magnetometry data shows an apparent 'soft magnetic phase', which is strongest in high Ru content films indicating a canting of the net moment in zero field.

The findings support the hypothesis of presence of intra-sublattice competition of positive nearest and negative next nearest neighbour exchanges on the Mn^{4c} sublattice. The "soft component" of the net moment observed in the SQUID data could arise from Mn^{4c} sublattice moments canting away from the anisotropy axis forming an easy cone, which is closed when an external field is applied. Initial analysis of XMCD data which allow to construct 2-D projection of site specific Mn moments supports this hypothesis. The data at zero fields shows small canting of the sublattice moments, which results in a large canting angle of the net moment of up to $\approx 50^\circ$. The XMCD study will be the subject of a future publication.

Addition of Ru decreases θ_{AH} and hence the extrinsic spin-orbit scattering contributions cannot explain the high values observed. The Mn^{4c} sublattice dominates transport and breaks inversion symmetry, allowing for a non-collinear spin texture. The high values of θ_{AH} can originate from the intrinsic contribution to AHE.

Varying the Mn and Ru content of MRG thin films identified compositions with high degree of crystallinity, high spin polarisation, enormous anisotropy fields in excess of 12 T near compensation and large θ_{AH} of 2.0%. The results also revealed possibilities of non-collinearity of sublattice moments and a non-collinear spin texture, which could be investigated further by XMCD and neutron diffraction.

ACKNOWLEDGMENTS

K.E.S. and J.M.D.C. acknowledge funding through Irish Research Council under Grant GOIPG/2016/308 and in part by the Science Foundation Ireland under Grant 12/RC/2278. G.A., A.J. R.S. S.L., J. O'B., P.S. and K.R. would like to acknowledge funding from TRANSPiRE FET Open Programme, H2020. K.E. acknowledges funding from Science Foundation Ireland US-Ireland R&D (Center-to-Center) under grant 16/USC2C/3287. N.T. was supported by the European Union's Horizon 2020 Research and Innovation Programme under Marie-Sklodowska Curie EDGE Grant 713567.

* siewierk@ted.ie

¹ H. van Leuken and R. A. de Groot, "Half-metallic antiferromag-

nets," *Phys. Rev. Lett.*, vol. 74, no. 7, pp. 1171–1173, 1995.

² T. Graf, C. Felser, and S. S. Parkin, "Simple rules for the under-

- standing of heusler compounds,” *Prog. Solid State Ch.*, vol. 39, no. 1, pp. 1 – 50, 2011.
- ³ H. Kurt, K. Rode, P. Stamenov, M. Venkatesan, Y. C. Lau, E. Fonda, and J. M. D. Coey, “Cubic Mn_2Ga thin films: Crossing the spin gap with ruthenium,” *Phys. Rev. Lett.*, vol. 112, no. 2, p. 027201, 2014.
 - ⁴ M. E. Jamer, Y. J. Wang, G. M. Stephen, I. J. McDonald, A. J. Grutter, G. E. Sterbinsky, D. A. Arena, J. A. Borchers, B. J. Kirby, L. H. Lewis, B. Barbiellini, A. Bansil, and D. Heiman, “Compensated ferrimagnetism in the zero-moment heusler alloy Mn_3Al ,” *Phys. Rev. Appl.*, vol. 7, no. 6, 2017.
 - ⁵ R. Stinshoff, G. H. Fecher, S. Chadov, A. K. Nayak, B. Balke, S. Ouardi, T. Nakamura, and C. Felser, “Half-metallic compensated ferrimagnetism with a tunable compensation point over a wide temperature range in the Mn-Fe-V-Al Heusler system,” *AIP Adv.*, vol. 7, no. 10, p. 105009, 2017.
 - ⁶ D. Betto, K. Rode, N. Thiyagarajah, Y.-C. Lau, K. Borisov, G. Atcheson, M. Žic, T. Archer, P. Stamenov, and J. M. D. Coey, “The zero-moment half metal: How could it change spin electronics?,” *AIP Adv.*, vol. 6, no. 5, p. 055601, 2016.
 - ⁷ G. Bonfiglio, K. Rode, K. Siewierska, J. Besbas, G. Y. P. Atcheson, P. Stamenov, J. M. D. Coey, A. V. Kimel, T. Rasing, and A. Kirilyuk, “Magnetization dynamics of the compensated ferrimagnet $\text{Mn}_2\text{Ru}_x\text{Ga}$,” *Phys. Rev. B*, vol. 100, p. 104438, Sep 2019.
 - ⁸ S. Lenne, Y.-C. Lau, A. Jha, G. Y. P. Atcheson, R. E. Troncoso, A. Brataas, J. M. D. Coey, P. Stamenov, and K. Rode, “Giant spin-orbit torque in a single ferrimagnetic metal layer,” 2019.
 - ⁹ K. E. Siewierska, N. Teichert, R. Schäfer, and J. M. D. Coey, “Imaging domains in a zero-moment half metal,” *IEEE Trans. Mag.*, vol. 55, no. 2, pp. 1–4, 2019.
 - ¹⁰ C. Banerjee, N. Teichert, K. Siewierska, Z. Gercsi, G. Atcheson, P. Stamenov, K. Rode, J. M. D. Coey, and J. Besbas, “Single pulse all-optical toggle switching of magnetization without Gd: The example of $\text{Mn}_2\text{Ru}_x\text{Ga}$,” 2019.
 - ¹¹ C. S. Davies, G. Bonfiglio, K. Rode, J. Besbas, C. Banerjee, P. Stamenov, J. M. D. Coey, A. V. Kimel, and A. Kirilyuk, “Exchange-driven all-optical magnetic switching in compensated 3d ferrimagnets,” *Phys. Rev. Research*, vol. 2, p. 032044, Aug 2020.
 - ¹² K. Borisov, D. Betto, Y. C. Lau, C. Fowley, A. Titova, N. Thiyagarajah, G. Atcheson, J. Lindner, A. M. Deac, J. M. D. Coey, P. Stamenov, and K. Rode, “Tunnelling magnetoresistance of the half-metallic compensated ferrimagnet mn_2ruxga ,” *Appl. Phys. Lett.*, vol. 108, no. 19, p. 192407, 2016.
 - ¹³ M. Žic, K. Rode, N. Thiyagarajah, Y.-C. Lau, D. Betto, J. M. D. Coey, S. Sanvito, K. J. O’Shea, C. A. Ferguson, D. A. MacLaren, and T. Archer, “Designing a fully compensated half-metallic ferrimagnet,” *Phys. Rev. B*, vol. 93, no. 14, p. 140202, 2016.
 - ¹⁴ N. Thiyagarajah, Y.-C. Lau, D. Betto, K. Borisov, J. M. D. Coey, P. Stamenov, and K. Rode, “Giant spontaneous Hall effect in zero-moment $\text{Mn}_2\text{Ru}_x\text{Ga}$,” *Appl. Phys. Lett.*, vol. 106, no. 12, p. 122402, 2015.
 - ¹⁵ P. Stamenov, “Point contact Andreev reflection from semimetallic bismuth—the roles of the minority carriers and the large spin-orbit coupling,” *J. Appl. Phys.*, vol. 113, no. 17, p. 17C718, 2013.
 - ¹⁶ K. Borisov, C.-Z. Chang, J. S. Moodera, and P. Stamenov, “High Fermi-level spin polarization in the $(\text{Bi}_{1-x}\text{Sb}_x)_2\text{Te}_3$ family of topological insulators: A point contact Andreev reflection study,” *Phys. Rev. B*, vol. 94, p. 094415, Sep 2016.
 - ¹⁷ I. V. Soldatov and R. Schäfer, “Advanced MOKE magnetometry in wide-field kerr-microscopy,” *J. Appl. Phys.*, vol. 122, no. 15, p. 153906, 2017.
 - ¹⁸ D. Betto, N. Thiyagarajah, Y.-C. Lau, C. Piamonteze, M.-A. Arrio, P. Stamenov, J. M. D. Coey, and K. Rode, “Site-specific magnetism of half-metallic $\text{Mn}_2\text{Ru}_x\text{Ga}$ thin films determined by x-ray absorption spectroscopy,” *Phys. Rev. B*, vol. 91, no. 9, p. 094410, 2015.
 - ¹⁹ B. Balke, S. Wurmehl, G. H. Fecher, C. Felser, and J. Kübler, “Rational design of new materials for spintronics: Co_2FeZ ($\text{Z}=\text{Al}, \text{Ga}, \text{Si}, \text{Ge}$),” *Sci. Technol. Adv. Mat.*, vol. 9, no. 1, p. 014102, 2008. PMID: 27877928.
 - ²⁰ N. Nagaosa, J. Sinova, S. Onoda, A. H. MacDonald, and N. P. Ong, “Anomalous Hall effect,” *Rev. Mod. Phys.*, vol. 82, no. 2, pp. 1539–1592, 2010.
 - ²¹ O. Meshcheriakova, S. Chadov, A. K. Nayak, U. K. Rößler, J. Kübler, G. André, A. A. Tsirlin, J. Kiss, S. Hausdorf, A. Kalache, W. Schnelle, M. Nicklas, and C. Felser, “Large non-collinearity and spin reorientation in the novel Mn_2RhSn Heusler magnet,” *Phys. Rev. Lett.*, vol. 113, p. 087203, Aug 2014.
 - ²² J. Železný, H. Gao, A. Manchon, F. Freimuth, Y. Mokrousov, J. Zemen, J. Mašek, J. Sinova, and T. Jungwirth, “Spin-orbit torques in locally and globally noncentrosymmetric crystals: Antiferromagnets and ferromagnets,” *Physical Review B*, vol. 95, no. 1, p. 22, 2017.
 - ²³ C. Sürgers, W. Kittler, T. Wolf, and H. v. Löhneysen, “Anomalous hall effect in the noncollinear antiferromagnet mn_5si_3 ,” *AIP Advances*, vol. 6, no. 5, p. 055604, 2016.
 - ²⁴ T. Seki, S. Iihama, T. Taniguchi, and K. Takahashi, “Large spin anomalous Hall effect in $\text{L1}_0\text{-FePt}$: Symmetry and magnetization switching,” *Phys. Rev. B*, vol. 100, p. 144427, Oct 2019.